Journal of Materials Chemistry B

ROYAL SOCIETY OF CHEMISTRY

PAPER

View Article Online
View Journal | View Issue

Check for updates

Cite this: J. Mater. Chem. B, 2023, 11, 8657

A novel PEC and ECL bifunctional aptasensor based on V_2CT_x MXene-derived MOF embedded with silver nanoparticles for selectively aptasensing miRNA-126†

Yu Li,[a] Shuai Zhang,[b] Mengfei Wang,[b] Chuanpan Guo,[b] Zhihong Zhang *[b] and Nan Zhou*[a]

A novel photoelectrochemical (PEC) and electrochemiluminescence (ECL) bifunctional aptasensor has been established for the detection of miRNA-126 using V_2CT_x MXene-derived porphyrin-based metal–organic framework embedded with Ag nanoparticles (Ag NPs) (denoted as AgNPs@V-PMOF) as a robust bioplatform. Due to the presence of V nodes in V_2CT_x MXene nanosheets, V-based MOF was prepared using tetrakis(4-carboxyphenyl)porphyrin as ligand, followed by the incorporation of Ag^+ ions to form the AgNPs@V-PMOF Schottky heterojunction. Benefiting from the fast electron transfer of the V_2CT_x substrate and well-matched band-edge energy level of the photosensitive Ag NPs and V-PMOF, the constructed AgNPs@V-PMOF Schottky heterojunction exhibited the promoted transfer of the photo-generated carriers, showing superior PEC and ECL performances. Moreover, a large number of the complementary DNA strand of miRNA-126 can be immobilized over AgNPs@V-PMOF in view of the combined interaction of π–π stacking, van der Waals force, and Ag–N coordination between AgNPs@V-PMOF. Consequently, the developed AgNPs@V-PMOF-based aptasensor illustrated extremely low detection limits of 0.78 and 0.53 fM within a wide range from 1.0 fM to 1.0 nM of miRNA-126 detected by PEC and ECL techniques, respectively, superior to most reported miRNA aptasensors. Also, the provided bifunctional aptasensor demonstrated high selectivity, good stability, fine reproducibility, and acceptable regenerability, as well as promising potential for the analysis of miRNA-126 from living cancer cells. This work puts forward the development of aptasensors for the early and accurate diagnosis of cancer markers and extends the application of MOF in the biosensing field.

Received 18th June 2023,
Accepted 10th August 2023

DOI: 10.1039/d3tb01380d

rsc.li/materials-b

Published on 19 avgust 2023. Downloaded on 20. 06. 2025 13:56:39.

Introduction

MicroRNA (miRNAs), small single-stranded non-coding RNAs with 18–25 nucleotides, which play the critical role as regulators of a variety of biological processes, are often regarded as a category of important cancer markers.[1] Thus, cancer-specific miRNAs such as miRNA-126, miRNA-141, miRNA-210, miRNA-21, miRNA-155, miRNA let-7a, miR-203, and miRNA-133a can be regarded as biomarkers for the inspection of cancers, such as primary glioblastoma, breast carcinoma, lung cancer, and hepatocellular carcinoma.[2] Therefore, it is essential to exploit an early and sensitive method to detect miRNAs with low levels in human serum or overexpressed in living cancer cells, which can remarkably enhance the therapy efficiency of diverse diseases.[3] Various biosensors have been established by combining different determination techniques, such as photoelectrochemical (PEC),[4] electrochemical,[5] electrochemiluminescence (ECL),[6] polymerase chain reactions,[7] and fluorescence.[8] Most of the analysis strategies of miRNAs rely on sole-modal detection, which cannot ensure the detection accuracy.[9] In this esteem, the utilization of the biosensing strategy for the detection of one target using two different methods can provide a promising, advanced precise analysis strategy due to the integration of the advantages of two diverse methods.[10] In comparison, the bifunctional biosensing strategy can efficiently supply additional information that cannot be achieved with individual technology.[10,11] Nevertheless, only a few reports have been developed for the detection of miRNA, such as the coupling of ECL/electrochemical impedance spectroscopy (EIS)[12] and fluorescence/mass spectrometry.[13] ECL, which combines the merits of chemiluminescence and electrochemical techniques, is widely applied in the detection of miRNAs in light

[a] Department of Orthopaedic Surgery, The First Affiliated Hospital of Zhengzhou University, Zhengzhou 450002, P. R. China. E-mail: fcczhoun@zzu.edu.cn
[b] College of Material and Chemical Engineering, Zhengzhou University of Light Industry, Zhengzhou 450001, P. R. China. E-mail: 2006025@zzuli.edu.cn

† Electronic supplementary information (ESI) available: Methods, synthesis, characterization, and performance analysis. See DOI: https://doi.org/10.1039/d3tb01380d

Published on 19 avgust 2023. Downloaded on 20. 06. 2025 13:56:39.

of its superior detection sensitivity, wide linear range, high stability, and fast response.[14] Generally, the sensing principle of ECL sensor is based on the detection interaction between biological recognition elements and corresponding targets *via* emission intensity change of luminophores.[15,16] In addition, PEC biosensors have demonstrated the advantages of simple instrumentation, ultrahigh detection sensitivity, superior stability, and low background noise, also showing promising application for the analysis of trace miRNAs.[17] The detection mechanism of a PEC sensor is based on the photoelectric chemical effect, which refers to the photosensitive material excited under light stimulation, generating carriers and charge separation and transfer.[18,19] Considering the synergistic effects between the ECL and PEC biosensing methods, we have constructed the corresponding integrated method to accurately detect the ultralow-level miRNAs in biological systems.

With regard to the construction of PEC and ECL biosensors, the utilization of electrode materials with high photoelectric conversion efficiency and superior ECL performances is most important.[20] The currently used electrode materials often include graphitic carbon nitride, transition metal dichalcogenide, quantum dots, porous-organic frameworks, and semiconductor organic materials.[21] Metal–organic frameworks (MOFs), attained through the coordination bonds of metal ions or clusters and organic ligands, have demonstrated structure and property merits such as high porosity and surface area, tailorable structure, good functionality, and feasibility to embrace diverse components, as well as enhanced bioaffinity toward DNAs or aptamers.[22] A variety of MOFs have widely acted as sensitive platforms for the manufacture of different biosensors to detect biomarkers, such as Ru@UiO-66,[23] Cu-MOF@COF,[24] Au-NPs@Zn-MOF,[17] Au NPs/Yb-TCPP,[25] and $ZnIn_2S_4$@NH_2-MIL-125(Ti).[26] Particularly, in view of the superior optical, luminescent, and electrochemical properties of metal nodes and organic linkers in MOF networks, some MOFs such as Eu-MOF,[27] Ce-MOF,[28] Ru-MOF,[29] Zr-MOF,[30] and La-MOF[31] were developed as ECL emitters for the construction of ECL biosensors. Unfortunately, limited categories of luminescent MOFs have restrained the extensive applications of MOFs in ECL biosensing fields. To overcome this shortcoming, MOF networks also can serve as carriers for confining luminophores (such as Pd,[32] Ag,[33] their alloys[34] or organic molecules[35]) to enhance the ECL signal, demonstrating the increased amount of luminophores in light of the high porous skeleton and large pore sizes in MOFs in comparison with conventional nanomaterial-based ones.[36] In addition, due to their enhanced light absorption *via* multilight scattering/reflection, diverse kinds of pristine MOFs,[37] MOF-based composites,[38] and MOF-derived nanomaterials[39] have also served as photoactive materials for developing PEC biosensors to detect biomarkers. For instance, an efficient PEC biosensor was manufactured based on PCN-224, simultaneously utilizing the Ti_3C_2/$MgIn_2S_4$ heterojunction as the electrode for the detection of miRNA-21.[40] Given that most pristine MOFs-based PEC and ECL platforms suffer from the inferior photoelectric conversion efficient, low photoabsorption ability, electrochemical activity, and unstable luminescence performance, the development of MOF-based ECL and PEC biosensors for the detection of miRNAs is still in the infancy stage.

Among many MOFs, porphyrin-based MOFs (p-MOFs), which are constructed using porphyrin or metalloporphyrin as ligands, have attracted increasing interest owing to their promising performances in biological and photoelectric fields.[41] A variety of p-MOFs, such as PCN-224,[42] Cu-TCPP,[43] or Yb-TCPP[25] were employed as platforms for the construction of PEC biosensors, while Zn-TCPP,[44] Zr-TCPP,[45] or Cu-TCPP[46] were used as emitters for the development of ECL biosensors. Accordingly, it is highly promising to construct a novel bifunctional biosensor based on p-MOFs for the sensitive and selective determination of miRNA. Recently, two-dimensional (2D) p-MOF nanosheets (NSs) have been prepared using V_2CT_x MXene NSs as precursor and porphyrin as linking ligand[47] (denoted as V-PMOF). Benefiting from the features of V_2CT_x MXene (such as excellent conductive properties and charge-transfer kinetics) and p-MOFs (such as precise and tunable coordination environments of metal active sites, wide photoabsorption ability, and electrochemical performance), the gained V-PMOF demonstrated rich functionality, more metal active species, and boosted electrochemical activity.[47,48] Inspired by these pioneer reports, we have prepared a novel Schottky heterojunction established by incorporating Ag nanoparticles (NPs) into the V-PMOF networks (represented by AgNPs@V-PMOF) and employed it as the PEC and ECL bifunctional platform for the construction of a biosensor to analyse trace miRNA efficiently.

In this work, miRNA-126 was taken as an example, which is closely related to the malignancy and disease progression of non-small cell lung cancer. Although some electrochemical and ECL techniques have been used for the analysis of miRNA-126,[49] further efforts are still needed for the sensitive and accurate diagnosis of miRNA-126 overexpressed in cancer cells. As indicated in Scheme 1, the AgNPs@V-PMOF Schottky heterojunction was prepared using V_2CT_x MXene as a precursor and tetrakis(4-carboxyphenyl)porphyrin (TCPP) as linking ligand through the hydrothermal method. After that, Ag NPs were incorporated into the porous V-PMOF network, forming the AgNPs@V-PMOF Schottky heterojunction. The attained AgNPs@V-PMOF Schottky heterojunction not only exhibited enhanced photoabsorption performance within the visible-near-infrared (NIR) range and promoted the transfer of the photogenerated carriers due to the unique Schottky heterojunction and well-matched band-edge energy level, but also possessed the boosted ECL activity in light of the surface Plasmon resonance effect, accelerated electron transfer, and promoted the photocarrier density of Ag NPs. Thereby, the developed AgNPs@V-PMOF Schottky heterojunction can serve as a sensitive platform for the PEC and ECL bifunctional aptasensor for the accurate and efficient detection of miRNA-126 selectively. Within a wide range from 1.0 fM to 1.0 nM of miRNA-126, the developed AgNPs@V-PMOF-based PEC and ECL biosensor exhibited ultralow detection limits of 0.78 and 0.53 fM, respectively, outperforming most of the reported miRNA aptasensors. Given the superior selectivity, high stability, and good reproducibility, as well as the expectable outstanding probability of the constructed bifunctional aptasensor, it also demonstrated the

 This journal is © The Royal Society of Chemistry 2023

Published on 19 avgust 2023. Downloaded on 20. 06. 2025 13:56:39.

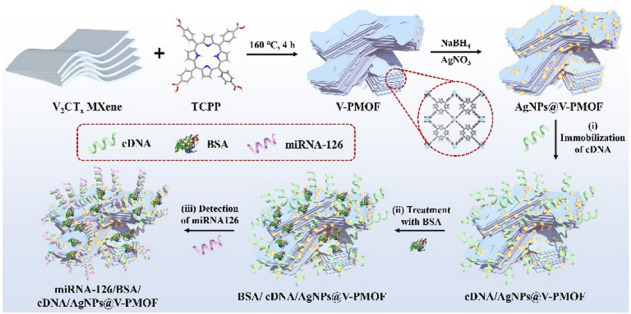

Scheme 1 Schematic illustration of the synthesis process of AgNPs@V-PMOF and fabrication of the PEC and ECL bifunctional aptasensor based on AgNPs@V-PMOF for the detection of miRNA-126, including (i) the immobilization of complementary DNA strands (cDNA/AgNPs@V-PMOF), (ii) the treatment with bovine serum albumin solution (BSA) (BSA/cDNA/AgNPs@V-PMOF), and (iii) the detection of miRNA-126 (miRNA-126/BSA/cDNA/AgNPs@V-PMOF).

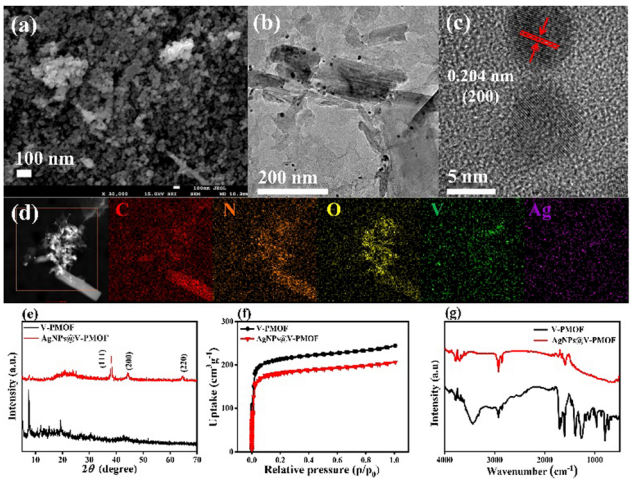

Fig. 1 (a) SEM image, (b) and (c) TEM and HR-TEM images, and (d) HAADF-STEM EDS element mapping image of AgNPs@V-PMOF, including C (red), N (orange), O (yellow), V (green) and Ag (purple). (e) PXRD pattern, (f) N_2 adsorption–desorption isotherms, and (g) FT-IR spectra of V-PMOF and AgNPs@V-PMOF.

promising practical application for the sensitive determination of miRNA overexpressed in living cancer cells. The present work proposes a novel integrated detection approach based on the MOF-based composite for the sensitive and selective analysis of miRNAs from living cancer cells, thus showing the potential application in the clinical diagnosis of cancers.

Results and discussion

Nanostructure and chemical component of the AgNPs@V-PMOF hybrid

As depicted in Fig. S1a (ESI†), V-PMOF illustrated the irregular nanoflake-like shape, which was loosely stacked together. The transmission electron microscope (TEM) image (Fig. S1b, ESI†) further verified the nanosheet-like structure of V-PMOF, consistent with the previous work.[50] The high-resolution TEM (HR-TEM) image of V-PMOF (Fig. S1c, ESI†) demonstrated a clear lattice fringe with a space of 0.41 nm, which was in line with the (006) plane of V_2CT_x.[51] Further, the high-angle annular dark-field scanning transmission electron microscopy (HAADF-STEM) and the energy-dispersive X-ray spectroscopy (EDS) of V-PMOF (Fig. S1d, ESI†) indicated the coexistence of V, C, N, and O elements with homogeneous distribution within a selected region. Moreover, the field emission scanning electron microscope (FE-SEM) image (Fig. 1(a)) displayed the AgNPs@V-PMOF hybrid composed of large amounts of NPs. This finding revealed that the Ag doping changed the nanostructure of V-PMOF significantly. The TEM image of AgNPs@V-PMOF (Fig. 1(b)) indicated that some NPs were embedded within ultrathin NSs, suggesting the combination of Ag NPs with V-PMOF NSs. The HR-TEM image of AgNPs@V-PMOF (Fig. 1(c)) hinted at the lattice fringe of 0.204 nm, which was attributed to the (200) plane of Ag NPs. In addition, the HAADF-STEM EDS mapping image of AgNPs@V-PMOF (Fig. 1(d)) illustrated the uniform dispersion of Ag, V, C, N, and O elements within the selected region.

The powder X-ray diffraction (PXRD) pattern of V-PMOF (Fig. 1(e)) shows the diffraction peaks at 2θ = 7.5°, 10.7°, 11.8°, 15.1°, and 19.4°, suggesting the successful preparation of V-PMOF.[52] With respect to AgNPs@V-PMOF, the XRD pattern demonstrated one main peak at 2θ = 7.5°, along with the other three insignificant peaks at 2θ = 38.1°, 44.2°, and 64.4° due to (111), (200), and (220) planes of Ag NPs, respectively. These results were consistent with the TEM results, confirming the embracement of Ag NPs into the porous V-PMOF network. The N_2 sorption–desorption isotherms of V-PMOF and AgNPs@V-PMOF displayed a type-I reversible sorption profile (Fig. 1(f)), suggesting their microporous structure. The Brunauer–Emmett–Teller surface area of AgNPs@V-PMOF was around 671 $m^2\ g^{-1}$, lower than that of V-PMOF (802 $m^2\ g^{-1}$) due to the pore filling by Ag NPs. As shown in Fig. 1(g), an additional peak at 530 cm^{-1} due to Ag_2O was observed in the FT-IR spectrum of AgNPs@V-PMOF besides the characteristic peaks of V-PMOF, verifying the presence of Ag NPs.

The X-ray photoelectron spectroscopy (XPS) survey scan spectrum of AgNPs@V-PMOF (Fig. S2, ESI†) included the Ag 3d (367.7 eV), V 2p (572.6 eV), C 1s (284.6 eV), N 1s (400 eV), and O 1s (530 eV) signals, while Ag 3d XPS signal was absent in the XPS spectrum of V-PMOF. The high-resolution C 1s XPS spectrum of AgNPs@V-PMOF (Fig. 2(a)) was composed of C=C, C–C, C–N, C–O, and COO, resembling those of V-PMOF. The N 1s XPS spectra of V-PMOF were fitted to pyridinic N, graphitic N, and NO_x (Fig. S3, ESI†). In addition, both pyridinic N and pyrrolic N were found in AgNPs@V-PMOF. Additionally, the V 2p XPS spectra of V-PMOF and AgNPs@V-PMOF (Fig. 2(b)) were deconvoluted into two main peaks of V $2p_{3/2}$ and V $2p_{1/2}$. The V $2p_{3/2}$ peak of V-PMOF was fitted into V^{4+} and V^{5+}, hinting at the mixed metal valence states. The Ag 3d XPS spectrum of AgNPs@V-PMOF (Fig. 2(c)) was separated into two couples of Ag $3d_{5/2}$ and Ag $3d_{3/2}$, which comprised the metallic Ag^0 (367.8 and 373.8 eV), together with two small peaks of Ag^+ ions in Ag_2O (368.6 and 374.4 eV). This result displayed that Ag species were

Published on 19 avgust 2023. Downloaded on 20. 06. 2025 13:56:39.

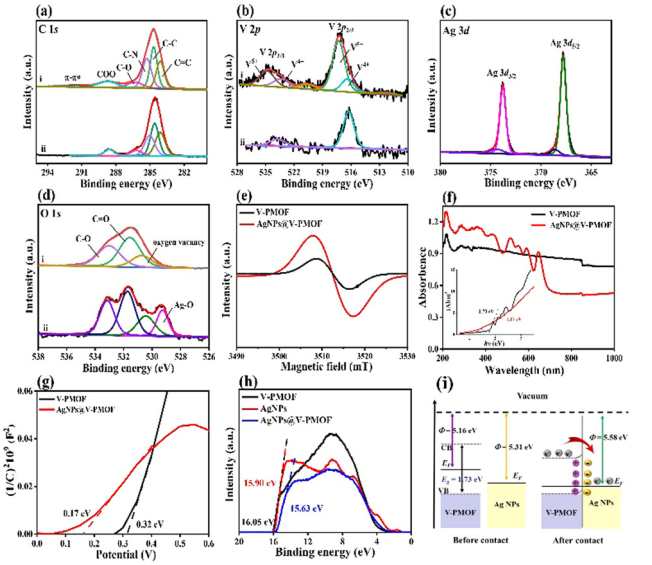

Fig. 2 High-resolution (a) C 1s, (b) V 2p, (c) Ag 3d, and (d) O 1s XPS spectra of (i) V-PMOF and (ii) AgNPs@V-PMOF. (e) EPR spectra, (f) UV-vis diffuse reflectance spectroscopy and the plots of $(\alpha h\nu)^2$ *versus* photo-energy ($h\nu$) (inset), and (g) Mott–Schottky curves of V-PMOF and AgNPs@V-PMOF. (h) UPS spectra of V-PMOF, Ag NPs, and AgNPs@V-PMOF. (i) Schematic illustration of the band structure and internal electric field at the interface of AgNPs@V-PMOF Schottky heterojunction.

partially oxidized to Ag_2O, consistent with the Fourier transform infrared (FT-IR) spectrum. The O 1s XPS spectrum of V-PMOF was separated into oxygen vacancy, C═O, and C–O (Fig. 2(d)). Nevertheless, an additional group of Ag–O (529.2 eV) was found in the O 1s XPS spectrum of AgNPs@V-PMOF. This appearance suggested that the incorporation of Ag species can introduce oxygen vacancy, beneficial to the improvement of photoabsorption ability and electron transfer.[52] The EPR spectrum of V-PMOF (Fig. 2(e)) shows a clear signal at g = 2.004, demonstrating the intrinsic detects. As V_2CT_x MXene was used as a precursor for the preparation of V-PMOF, the V clusters fastened among the V_2CT_x lattice restrain the single crystal growth, resulting in defects within V-PMOF.[51] As compared, the EPR signal of AgNPs@V-PMOF was significantly higher than that of V-PMOF, demonstrating plenty of element vacancies. The highly defective nanostructure of AgNPs@V-PMOF benefits the improvement of photoabsorption and electron transfer.[53]

Optical and electrochemical properties of the AgNPs@V-PMOF Schottky heterojunction

The photoabsorption abilities of V-PMOF and AgNPs@V-PMOF were characterized by UV-vis diffuse reflectance spectroscopy (DRS) (Fig. 2(f)), which indicated a wide absorption within the UV-vis-NIR range. However, AgNPs@V-PMOF exhibited an optical absorption edge of around 650 nm, accompanying with a series of absorption peaks in the UV and visible light regions. The enhanced UV-vis light absorption ability of AgNPs@V-PMOF was mainly due to the contribution of Ag NPs. The band gap energy (E_g) of AgNPs@V-PMOF, which was deduced by plotting $(\alpha h\nu)^2$ *versus* photo-energy ($h\nu$), was calculated to be 1.17 eV, remarkably lower than that of V-PMOF (1.73 eV). Moreover, the Mott–Schottky plots of the two samples (Fig. 2(g)) showed positive slopes, indicating their n-type semiconductor properties. According to the Mott–Schottky plot of V-PMOF, the flat band position was estimated to be 0.32 V *vs.* Ag/AgCl or 0.52 V *vs.* normal hydrogen electrode (NHE), higher than that of AgNPs@V-PMOF (0.37 V *vs.* NHE). Consequently, the energy level of the conduction band (E_{CB}) of V-PMOF was 0.42 V *vs.* NHE, whereas the energy level of the valence band (E_{VB}) was 2.15 V *vs.* NHE, which was calculated by the formula ($E_{VB} = E_{CB} + E_g$). The steady-state photoluminescence (PL) spectra (Fig. S4a, ESI†) demonstrated that the peak intensity of AgNPs@V-PMOF was lower than that of V-PMOF, showing a blue shift from 640 nm to 613 nm. These results further confirmed that the incorporation of Ag NPs into V-PMOF networks can efficiently suppress the recombination of photocarriers. In addition, the charge transfer and photocurrent response of the two samples were further measured by the EIS technique (Fig. S4b, ESI†). It is clear that the resistance of charge transfer (R_{ct}, 168 Ω) of AgNPs@V-PMOF was smaller than that of V-PMOF (533 Ω). It hinted that the Ag doping into V-PMOF could markedly enhance electron transfer. As depicted in Fig. S4c (ESI†), the photocurrent of AgNPs@V-PMOF was 0.40 μA, slightly higher than that of V-PMOF (0.35 μA) and significantly larger than that of the bare glass carbon electrode (GCE, 4 nA). Consequently, the introduction of Ag NPs into the V-PMOF network can promote the separation of photo-generated electrons and holes, amplifying the photoelectronic performance.

The work function (Φ, energy difference between vacuum level and Fermi level) of the AgNPs@V-PMOF heterojunction was determined by ultraviolet photoelectron spectroscopy (UPS). Fig. 2(h) shows the secondary electron cutoff energies (E_{cutoff}) of V-PMOF, Ag NPs, and AgNPs@V-PMOF to be around 16.05, 15.90, and 15.63 eV, respectively. As such, by subtracting the E_{cutoff} from the excitation energy of 21.21 eV,[54] Φ for V-PMOF (5.16 eV) and Ag NPs (5.31 eV) are obtained. As illustrated in Fig. 2(i), the E_F of V-PMOF was higher than that of Ag NPs, AgNPs@V-PMOF was calculated to be 5.58 eV, which is higher and suggests a Schottky heterojunction can be formed between the two components.[55] After contact between the two sole components, electrons flowed from V-PMOF to Ag NPs until an equilibrium was reached, generating positive charges and an upward bend in the band edge of the V-PMOF surface. Meanwhile, electrons accumulated on the Ag NPs surface, resulting in the establishment of an internal built-in electric field from V-PMOF to Ag NPs. Under visible light irradiation, the photo-induced electrons on CB of V-PMOF fast migrated to Ag NPs. The Schottky barrier remarkably impeded the backflow of electrons, resulting in efficient separation and transfer of photo-generated carriers.

The sensing performance of the PEC and ECL bifunctional aptasensor toward miRNA-126

To investigate the ECL mechanism, ECL-potential profiles of the electrodes modified by V-PMOF and AgNPs@V-PMOF were measured with a cyclic potential scanning range of −2 to 0 V in a 5 mM $S_2O_8^{2-}$ solution system. As shown in Fig. S5 (ESI†), the

 This journal is © The Royal Society of Chemistry 2023

Published on 19 avgust 2023. Downloaded on 20. 06. 2025 13:56:39.

bare GCE exhibited no ECL intensity. A significant ECL peak with an intensity of 4299 a.u. was observed for the V-PMOF/GCE, ascribing to the emission of the excited state of V-PMOF (^{1}V-PMOF*). In comparison, AgNPs@V-PMOF/GCE exhibited a remarkably enhanced ECL intensity. As coreaction accelerators, Ag NPs can boost the cathodic ECL signal and effectively amplify the ECL response.[56] In the presence of Ag NPs, more oxidants, $SO_4^{\bullet -}$, can be generated by the electrochemical reduction of $S_2O_8^{2-}$, boosting the ECL signal of the modified electrode.

The development procedure of the AgNPs@V-PMOF-based ECL biosensor and the detection of miRNA-126 was recorded by ECL measurement in phosphate buffer saline (PBS, 0.01 M, pH 7.4). As demonstrated in Fig. S6a (ESI†) (curve ii), the cDNA/AgNPs@V-PMOF/GCE demonstrated an evidently reduced ECL signal in comparison with the AgNPs@V-PMOF/GCE. It was due to the steric hindrance of the anchored cDNA strands. After blocking the aptasensor with BSA, a slight decrease in the ECL intensity of the BSA/cDNA/AgNPs@V-PMOF/GCE was attained (curve iii, Fig. S6a, ESI†). It suggested that only negligible non-specific adsorption occurred between the target and AgNPs@V-PMOF. When detecting miRNA-126, the ECL peak of the miRNA-126/BSA/cDNA/AgNPs@V-PMOF/GCE (curve vi) declined continuously. As reported, the hybridized double strands can be yielded between cDNA and miRNA-126, further hampering electron transfer at the electrode/electrolyte. Similarly, the procedures of the construction of the biosensor and detection of miRNA-126 were also studied by the EIS technique (Fig. S6b, ESI†). The adsorption of cDNA over the cDNA/AgNPs@V-PMOF/GCE (521 Ω) resulted in an increase in R_{ct} relative to the AgNPs@V-PMOF/GCE (168 Ω). It showed that the insulated cDNA layer over the modified electrode substantially inhibited the electron transfer from the electrolyte to the electrode due to steric hindrance. Similarly, the adsorption of BSA on cDNA/AgNPs@V-PMOF/GCE only caused the inconspicuous increase in R_{ct} due to the indiscernible non-specific adsorption. However, the detection of miRNA-126 using the AgNPs@V-PMOF-based biosensor further led to an apparent increase in R_{ct} (913 Ω), which was assigned to the hindrance of electron transfer of the formed double strand cDNA/miRNA-126.

As aforementioned, the established AgNPs@V-PMOF Schottky heterojunction demonstrated superior photoelectric conversion efficiency. Besides the ECL biosensor, one can anticipate developing the PEC biosensor for the detection of miRNA-126. Fig. 3(a) indicates the photocurrent variation of the step-by-step construction for manufacturing the PEC biosensor. After cDNA immobilization, the photocurrent of the modified electrode declined from 0.40 to 0.34 μA. Apparently, the steric hindrance between the photosensitive material and the electrolyte caused by the cDNA anchoring further inhibited electron transfer and photoactivity. Almost all active sites in AgNPs@V-PMOF were occupied by cDNA, leading to the extremely poor non-specific binding with miRNA-126. Moreover, the BSA blocking resulted only in a slight variation of the photocurrent of the modified electrode, again confirming the ignorable non-specific binding of BSA. When detecting miRNA-126 by the constructed PEC biosensor, the continuous decline in the photocurrent of the electrode was observed. This appearance also originated from the insulated

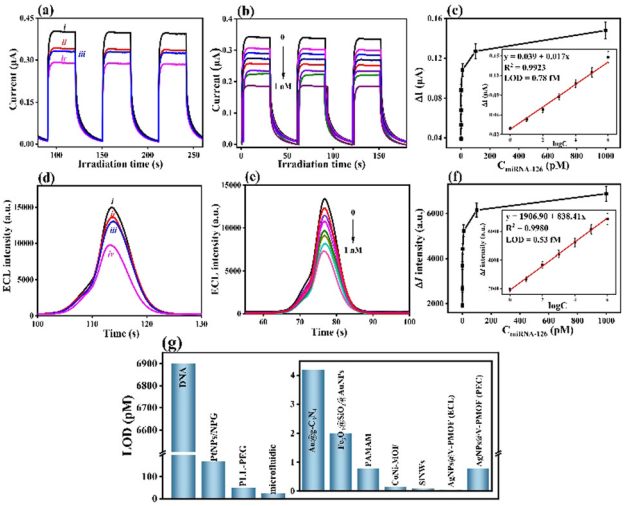

Fig. 3 (a) Photocurrent responses of diverse electrodes in 0.01 M PBS, including the (i) AgNPs@V-PMOF/GCE, (ii) cDNA/AgNPs@V-PMOF/GCE, (iii) BSA/cDNA/AgNPs@V-PMOF/GCE, and (iv) miRNA-126/BSA/cDNA/AgNPs@V-PMOF/GCE. (b) Photocurrent densities caused by the detection of miRNA-126 with different concentrations (from top to bottom: 1.0 fM, 10 fM, 100 fM, 1 pM, 10 pM, 100 pM, and 1 nM) using the AgNPs@V-PMOF-based biosensor. (c) Calibration curve between ΔI and the miRNA-126 concentration (inset: the linear fit plot of ΔI as a function of the logarithm of the miRNA-126 concentration). (d) ECL intensities of diverse electrodes in 0.01 M PBS, including (i) AgNPs@V-PMOF/GCE, (ii) cDNA/AgNPs@V-PMOF/GCE, (iii) BSA/cDNA/AgNPs@V-PMOF/GCE, and (iv) miRNA-126/BSA/cDNA/AgNPs@V-PMOF/GCE. (e) Photocurrent responses caused by the detection of miRNA-126 with different concentrations using the AgNPs@V-PMOF-based biosensor. (f) Calibration curve between ΔI and the miRNA-126 concentration (inset: the linear fit plot of ΔI as a function of the logarithm of the miRNA-126 concentration). The error bars are standard deviations for n = 3. (g) Comparison of the LOD of the developed aptasensor with other reported biosensors.

performance and steric hindrance of the hybridized double stranded strands formed between miRNA-126 and cDNA. As indicated in Fig. S7a (ESI†), the C 1s XPS spectra of cDNA/AgNPs@V-PMOF involved C=C, C–C, C–O, and N–C=O, as well as K^+ ions. Among them, the high content C–C and the presence of N–C=O originated from cDNA, while K^+ ions were caused by the residual of PBS. Importantly, the apparent P 2p XPS signal (Fig. S7b, ESI†) further proved the cDNA immobilization, which is composed of P $2p_{3/2}$ and P $2p_{1/2}$.

As depicted in Fig. S9 and described in the S3 section (ESI†), the optimal conditions for the analysis of miRNA-126 included the dosage of AgNPs@V-PMOF of 2 mg mL^{-1}, cDNA concentration of 100 nM, incubation time of cDNA of 0.5 h, and hybridization time of miRNA-126 with cDNA of 1 h.

Quantitative analysis of miRNA-126 using the PEC and ECL bifunctional aptasensor

To quantitatively analyse the biosensing ability for the inspection of miRNA-126, the fabricated PEC biosensor was incubated with a series of concentrations of miRNA-126 under optimal conditions. The separately recorded corresponding photocurrent responses are shown in Fig. 3(b), in which the obtained change in the photocurrent response ($\Delta I = I_{\text{miRNA-126}} - I_{\text{cDNA}}$)

Published on 19 avgust 2023. Downloaded on 20. 06. 2025 13:56:39.

gradually decreased with increasing miRNA-126 concentration from 1.0 fM to 1.0 nM. When the concentration of miRNA-126 was larger than 0.1 nM, the obtained ΔI approached a platform (Fig. 3(c)). A good linear relationship was attained from the calibration plot (inset, Fig. 3(c)) between the caused photocurrent signal (ΔI) and the logarithm of miRNA-126 concentrations ($\log con_{miRNA\text{-}126}$). The linear equation was represented as $\Delta I(\mu A) = 0.017 \log con_{miRNA\text{-}126} + 0.039$ toward miRNA-126 with the correlation coefficient $R^2 = 0.9924$. At a signal-to-noise ratio (S/N) of 3, an ultralow limit of detection (LOD) of 0.78 fM ($3s$/slope, where s represented the standard deviation of the blank sample) for the constructed PEC biosensor was gained within a range from 1.0 fM to 1.0 nM of miRNA-126.

Likely, the BSA/cDNA/AgNPs@V-PMOF/GCE was exposed to various concentrations of miRNA-126, for which the corresponding ECL responses were achieved (Fig. 3(d)). The variation in the ECL intensities (ΔI) decreased with increasing miRNA-126 concentration ranging from 1.0 fM to 1.0 nM (Fig. 3(e)). Accordingly, the linear equation was fitted as ΔI (a.u.) = $838.41 \log con_{miRNA\text{-}126} + 1906.90$ ($R^2 = 0.9980$) (Fig. 3(f)), giving an ultralow LOD of 0.53 fM (S/N = 3) within a wide range of 1.0 fM to 1.0 nM.

As compared with some reported miRNA biosensors (Table S1, ESI† and Fig. 3(g)), the established bifunctional aptasensor exhibited superior biosensing performance due to substantially lower LOD and wider linear range. MOFs or MOF derivatives often exhibit large specific surface area and pore size, high functionality, and enhanced bioaffinity toward probes (such as antibodies, DNAs, or aptamers). It thus can result in the immobilization of large amounts of probes *via* the combined interaction of electrostatic interaction, van der Waals forces, π–π* stacking, and metal-N binding *via* the two ways, including the adsorption on the surface and penetration into the interior channels of MOF-based materials. In this work, the excellent sensing ability can be attributed to the following factors: (i) the incorporation of Ag NPs within the V-PMOF network lowered the Femi level of V active sites, enhanced the electron and carrier transfer, boosted the separation ability of photogenerated electrons and holes, and regulated the photoabsorption performance, thus enlarging the photoelectric conversion efficiency and ECL performance; (ii) rich defects, large specific surface area and pore size, high functionality, and the surface plasmon resonance effect of Ag NPs in AgNPs@V-PMOF remarkably strengthened the cDNA immobilization, further improving the detection sensitivity of miRNA-126; (iii) the multiple binding force generated between cDNA and AgNPs@V-PMOF, such as π–π stacking, van der Waals force, and Ag–N coordination, endowed the tight anchoring of cDNA and declined the non-specific adsorption between the target and sensitive layer.

Selectivity, stability, and reproducibility of the developed bifunctional aptasensor

The selectivity of a biosensor is key for extensively broadening its practicality in diverse real samples. The constructed AgNPs@V-PMOF-based biosensor was separately incubated in diverse interferent solutions or dispersions, as well as their mixture with miRNA-126 and measured using PEC or ECL techniques. Their concentration was 100-fold of miRNA-126. As depicted in Fig. 4(a) and Fig. S10a (ESI†), the achieved PEC and ECL responses for the analysis of the interferent were pretty insignificant, while the detection of miRNA-126 resulted in remarkably high signals. Furthermore, the analysis of the mixture using the developed biosensor gave comparable signals, around 98.3% and 97.9% of the detection of miRNA-126 using PEC and ECL techniques, respectively. These appearances definitely clarified that the AgNPs@V-PMOF-based biosensor demonstrated high selectivity even in a complex environment. In addition, the five electrodes were utilized to develop the AgNPs@V-PMOF-based biosensor by the same method for the detection of miRNA-126 and separately by PEC and ECL methods. Fig. 4(b) and Fig. S10b (ESI†) indicate that the comparative PEC and ECL responses were found, illustrating relative standard deviations (RSDs) of 2.32% and 3.83%, respectively, verifying the excellent reproducibility of the established biosensor. The stability of the developed biosensor was assessed by recording the determined signals for the detection of miRNA-126 once per day and continuously for 14 days. As indicated in Fig. 4(c) and Fig. S10c (ESI†), the PEC and ECL signals obtained from the analysis of miRNA-126 illustrated close values, showing the RSDs of 3.03% and 3.19%, respectively. It thus proved that the manufactured biosensor shows good storage stability. Moreover, the regeneration ability of the proposed biosensor was also assessed. Fig. 4(d) and Fig. S10d (ESI†) show repeatable PEC and ECL responses to the detection of miRNA-126. After 10 runs, the recorded PEC and ECL signals maintained 97.2% and 101.5% of the initial values, respectively, revealing the promising regeneration performance of the bifunctional biosensor.

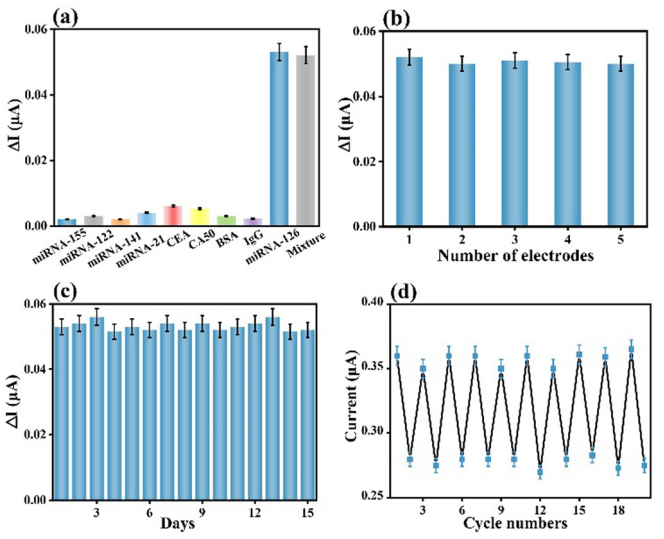

Fig. 4 (a) Selectivity of the constructed AgNPs@V-PMOF-based PEC biosensor for the detection of miRNA-126 (10 fM) in the presence of miRNA-155, miRNA-122, miRNA-141, miRNA-21, carcinoembryonic antigen (CEA), carbohydrate antigen 50 (CA50), BSA, and immunoglobulin G (IgG) (1 pM), and their mixture with miRNA-126. (b) Reproducibility, (c) storage stability, and (d) regenerability of the developed AgNPs@V-PMOF-based PEC biosensor for the analysis of miRNA-126 (100 fM). The error bars represented average standard errors for three measurements (n = 3).

 This journal is © The Royal Society of Chemistry 2023

Published on 19 avgust 2023. Downloaded on 20. 06. 2025 13:56:39.

In vitro practicality of the developed biosensor

As shown in Tables S2 and S3 (ESI†), it demonstrated that the acceptable recoveries ranged from 94.66% to 115.36%, together with the low RSD of 1.34% to 3.58%, respectively, inspected by the PEC and ECL techniques. Prior to the detection of miRNA-126 in living cells, the biocompatibility performances of AgNPs@V-PMOF in normal L929 cells and MCF-7 cells were investigated. As depicted in Fig. S11a and b (ESI†), the cell viabilities of L929 cells and MCF-7 cells were around 71.9% and 70.4% in the AgNPs@V-PMOF suspension (200 μg mL^{-1}), respectively. In addition, Fig. S11c (ESI†) indicated that the level of miRNA-126 in MCF-7 cells was approximately 50 times higher than those from L929 cells at the cell concentration of 1×10^5 cell mL^{-1}. These results connoted that the developed bifunctional biosensor based on AgNPs@V-PMOF exhibited wide and good feasibility in the determination of miRNA-126 in real samples.

Experimental

Preparation of the AgNPs@V-PMOF hybrid

V-PMOF was prepared according to the previous work.[57] With regard to the preparation of AgNPs@V-PMOF hybrid, 20 mg V-PMOF and 5.0 mg $AgNO_3$ were dissolved in 20 mL of Milli-Q water and thoroughly stirred for 5 min in the dark. After adding 2 mL of sodium borohydride (10 mg mL^{-1}), the mixture was continuously stirred for 4 h. Subsequently, the resultant mixture was centrifuged at 11 000 rpm, followed by rinsing with methanol three times. Finally, the black powder was dried at 60 °C in vacuum and represented as AgNPs@V-PMOF. In order to evaluate the effect of the ratio of Ag NPs to V-PMOF on the sensing performance, the two additional hybrids were prepared through a similar approach and using different dosages of $AgNO_3$ (1 and 10 mg) and denoted as AgNPs@V-PMOF-1 and AgNPs@V-PMOF-2, respectively.

Establishment of the AgNPs@V-PMOF-based aptasensor

The homogeneous AgNPs@V-PMOF suspensions with different concentrations (0.5, 1, 1.5, 2, and 2.5 mg mL^{-1}) were prepared by dispersing it (5, 10, 15, 20, and 25 mg) in Milli-Q water (10 mL) and subjecting to ultrasound for 10 min. After that, the bare GCE was modified by AgNPs@V-PMOF *via* the coating method (denoted as AgNPs@V-PMOF/GCE). After drying in air for 30 min. the attained AgNPs@V-PMOF/GCE was rinsed thoroughly with Milli-Q water thrice and dried again to remove the uncoated material. Due to ultrathin and highly conjugated nanostructure, AgNPs@V-PMOF can be intimately cohered with the bare GCE *via* van der Waals forces.[48] Subsequently, the AgNPs@V-PMOF/GCE was incubated with cDNA (100 nM) for 30 min (represented by cDNA/AgNPs@V-PMOF/GCE), followed by rinsing with phosphate buffer saline (PBS, 0.01 M, pH 7.4) thrice to remove the unanchored cDNA molecules, and dried in air for 1 h. Moreover, the blocking step was performed by incubating the obtained aptasensor in BSA (1 wt%) (denoted as BSA/cDNA/AgNPs@V-PMOF/GCE) to avoid the non-specific adsorption, followed by rinsing and dried again. The constructed biosensor was stored at 4 °C for the detection of miRNA-126.

Evaluation of the aptasensing performance of the proposed aptasensor

The LOD of the bifunctional biosensor was evaluated according to the previously reported work[48] by detecting miRNA-126 with different concentrations (1.0 fM, 10 fM, 100 fM, 1.0 pM, 10 pM, 0.1 nM, and 1.0 nM). Typically, a well-defined linear relationship was attained by taking the variations of these photocurrents and ECL responses before and after the detection of miRNA-126 as a function of the logarithm of the miRNA-126 concentration (log $C_{miRNA\text{-}126}$). According to the criterion as IUPAC recommended,[48] the LOD of miRNA-126 was assessed through the $3S_B/m$ equation, where S_B and m were the standard deviation of the blank (n = 11) and the slope of the linear calibration curve, respectively.

The selectivity of the developed aptasensor was apprised by comparing the caused photocurrent or ECL responses by the detection of miRNA-126 and interferents. Herein, diverse miRNAs (such as miRNA-155, miRNA-122, miRNA-141, and miRNA-21), other biomarkers (such as CEA, CA50), and proteins existing in human serum (such as BSA and IgG) were used as interferents to investigate the selectivity of the given aptasensor. The levels of these interferents were set as 1.0 pM, 100 times higher than that of miRNA-126 (10 fM). In addition, the stability, reproducibility, and regeneration ability of the developed bifunctional biosensor were assessed using a similar method to the reported work.[48]

Practicability of the developed bifunctional biosensor

Human serum from the First Affiliated Hospital of Zhengzhou University was used to study the applicability of the developed bifunctional biosensor after informed consent and permission of the patient and allowed by the ethical standards of the 1964 Declaration of Helsinki and its later amendments. Also, this proposal was agreed upon by the ethics committee of First Affiliated Hospital of Zhengzhou University. Further, the applicability of the constructed bifunctional biosensor was performed according to the standard addition method.[49] In addition, the applicability of the manufactured biosensor was also assessed *via* the detection of miRNA-21 overexpressed in normal L929 cells and MCF-7 cancer cells (100, 1×10^3, 1×10^4, and 1×10^5 cell mL^{-1}) using the same techniques as the above experiments.

In addition, the other experimental parts of materials and chemicals, preparation of all solutions, and basic characterizations are shown in the S1 Section (ESI†).

Conclusions

In summary, a novel PEC and ECL bifunctional biosensor for the sensitive and selective detection of miRNA-126 based on the AgNPs@V-PMOF Schottky heterojunction was constructed. As V_2CT_x-MXene-TCPP was *in situ* prepared from V_2CT_x substrate, it exhibited an ultrathin NS-like structure composed of plenty of defects and demonstrated enhanced photoabsorption ability. Further, the doped Ag species in V_2C-MXene-TCPP afforded

Published on 19 avgust 2023. Downloaded on 20. 06. 2025 13:56:39.

the regulated ability toward the V active sites, afforded surface plasmon resonance effect, accelerated electron transfer, promoted the photocarrier density, and enhanced the PEC and ECL response. In addition, large amounts of cDNA strands were immobilized over the AgNPs@V_2C-MXene-TCPP-modified GCE, and the constructed biosensor demonstrated an ultralow limit of detection of 0.78 and 0.53 fM deduced from the PEC and ECL techniques, within wide ranges from 1 fM to 1 nM, respectively. In view of excellent comprehensive aptasensing performance, the manufactured biosensor also displayed great application potential for the direct detection of miRNAs in living cancer cells. However, there are still some challenges to the widespread application of the constructed biosensor, such as the fussy preparation of the attained aptasensor, which includes multiple steps. Fortunately, this shortcoming can be overcome by the excellent regeneration ability of the gained biosensor. The present work can put forward the bifunctional biosensing strategy for the efficient detection of biomarkers in living cancer cells and also can extend the biosensing applications of MOF-based hybrids.

Conflicts of interest

There are no conflicts to declare.

Acknowledgements

The authors acknowledge funding from the Excellent Youth Science Foundation of Henan Province, China (no. 202300410494).

Notes and references

1 T. S. Zavvar, Z. Khoshbin, M. Ramezani, M. Alibolandi, K. Abnous and S. M. Taghdisi, *Biosens. Bioelectron.*, 2022, **214**, 114501.
2 N. Wang, J. Zhang, B. Xiao, X. Sun, R. Xie and A. Chen, *Biosens. Bioelectron.*, 2022, **211**, 114345.
3 C. Y. Song, Y. J. Yang, B. Y. Yang, Y. Z. Sun, Y. P. Zhao and L. H. Wang, *Nanoscale*, 2016, **8**, 17365–17373.
4 Q. Ding, M. Zhu, H. Deng, R. Yuan and Y. Yuan, *Biosens. Bioelectron.*, 2021, **184**, 113227.
5 L. Liu, S. Jiang, L. Wang, Z. Zhang and G. Xie, *Microchim. Acta*, 2015, **182**, 77–84.
6 J. Zhao, Y. He, K. Tan, J. Yang, S. Chen and R. Yuan, *Anal. Chem.*, 2021, **93**, 12400–12408.
7 P. Wang, F. Jing, G. Li, Z. Wu, Z. Cheng, J. Zhang, H. Zhang, C. Jia, Q. Jin, H. Mao and J. Zhao, *Biosens. Bioelectron.*, 2015, **74**, 836–842.
8 Y. Tu, W. Li, P. Wu, H. Zhang and C. Cai, *Anal. Chem.*, 2013, **85**, 2536–2542.
9 Y. Wu, Y. Zhang, X. Zhang, S. Luo, X. Yan, Y. Qiu, L. Zheng and L. Li, *Biosens. Bioelectron.*, 2021, **177**, 112962.
10 M. Liu, G. Chen, Y. Qin, J. Li, L. Hu, W. Gu and C. Zhu, *Anal. Chem.*, 2021, **93**, 9897–9903.
11 M. Li, H. Lin, S. K. Paidi, N. Mesyngier, S. Preheim and I. Barman, *ACS Sens.*, 2020, **5**, 1419–1426.
12 Y. Zheng, Y. Xu, L. Chen, X. Yin, F. Lin, S. Weng and X. Lin, *J. Electrochem. Soc.*, 2020, **167**, 167502.
13 H. Xu, Z. Zhang, Y. Wang, X. Zhang, J.-J. Zhu and Q. Min, *Anal. Chem.*, 2022, **94**, 6329–6337.
14 L. Yu, L. Zhu, M. Yan, S. Feng, J. Huang and X. Yang, *Anal. Chem.*, 2021, **93**, 11809–11815.
15 K. Wu, R. Chen, Z. Zhou, X. Chen, Y. Lv, J. Ma, Y. Shen, S. Liu and Y. Zhang, *Angew. Chem., Int. Ed.*, 2023, **62**, e202217078.
16 Y. Fang, Z. Zhou, Y. Hou, C. Wang, X. Cao, S. Liu, Y. Shen and Y. Zhang, *Anal. Chem.*, 2023, **95**, 6620–6628.
17 Q. Wei, C. Wang, X. Zhou, T. Wu, Y. Wang, C. Li and N. Yang, *Biosens. Bioelectron.*, 2019, **142**, 111540.
18 Q. Zhou, G. Li, K. Chen, H. Yang, M. Yang, Y. Zhang, Y. Wan, Y. Shen and Y. Zhang, *Anal. Chem.*, 2020, **92**, 983–990.
19 D. Han, X. Li, Z. Liang, B. Zhao, Z. Wu, F. Han, D. Han and L. Niu, *Chin. Chem. Lett.*, 2023, **34**, 107722.
20 Y. Zhao, L. Bouffier, G. Xu, G. Loget and N. Sojic, *Chem. Sci.*, 2022, **13**, 2528–2550.
21 Y. Chu, T. Han, A. Deng, L. Li and J.-J. Zhu, *TrAC, Trends Anal. Chem.*, 2020, **123**, 115745.
22 S. Zhang, F. Rong, C. Guo, F. Duan, L. He, M. Wang, Z. Zhang, M. Kang and M. Du, *Coord. Chem. Rev.*, 2021, **439**, 213948.
23 Y. Wang, H. Yin, X. Li, G. I. N. Waterhouse and S. Ai, *Biosens. Bioelectron.*, 2019, **131**, 163–170.
24 M. Xu, K. Chen, L. Zhu, S. Zhang, M. Wang, L. He, Z. Zhang and M. Du, *Langmuir*, 2021, **37**, 13479–13492.
25 Z. W. Jiang, T. T. Zhao, C. M. Li, Y. F. Li and C. Z. Huang, *ACS Appl. Mater. Interfaces*, 2021, **13**, 49754–49761.
26 T. Yan, T. Wu, S. Wei, H. Wang, M. Sun, L. Yan, Q. Wei and H. Ju, *Biosens. Bioelectron.*, 2020, **148**, 111739.
27 L. Zhao, M. Wang, X. Song, X. Liu, H. Ju, H. Ai, Q. Wei and D. Wu, *Chem. Eng. J.*, 2022, **434**, 134691.
28 Y. Zhou, J. He, C. Zhang, J. Li, X. Fu, W. Mao, W. Li and C. Yu, *ACS Appl. Mater. Interfaces*, 2020, **12**, 338–346.
29 G.-B. Hu, C.-Y. Xiong, W.-B. Liang, Y. Yang, L.-Y. Yao, W. Huang, W. Luo, R. Yuan and D.-R. Xiao, *Biosens. Bioelectron.*, 2019, **135**, 95–101.
30 L.-Y. Yao, F. Yang, G.-B. Hu, Y. Yang, W. Huang, W.-B. Liang, R. Yuan and D.-R. Xiao, *Biosens. Bioelectron.*, 2020, **155**, 112099.
31 H. Gao, X. Wei, M. Li, L. Wang, T. Wei and Z. Dai, *Small*, 2021, **17**, 2103424.
32 J. Fang, G. Zhao, X. Dong, X. Li, J. Miao, Q. Wei and W. Cao, *Biosens. Bioelectron.*, 2019, **142**, 2290–2295.
33 G. Mo, X. He, D. Qin, S. Meng, Y. Wu and B. Deng, *Biosens. Bioelectron.*, 2021, **178**, 113024.
34 B. He and X. Yan, *Sens. Actuators B Chem.*, 2020, **306**, 127558.
35 Y. Yang, G.-B. Hu, W.-B. Liang, L.-Y. Yao, W. Huang, Y.-J. Zhang, J.-L. Zhang, J.-M. Wang, R. Yuan and D.-R. Xiao, *Nanoscale*, 2020, **12**, 5932–5941.
36 X. Jiang, Z. Wang, H. Wang, Y. Zhuo, R. Yuan and Y. Chai, *Chem. Commun.*, 2017, **53**, 9705–9708.
37 G.-Y. Zhang, Y.-H. Zhuang, D. Shan, G.-F. Su, S. Cornier and X.-J. Zhang, *Anal. Chem.*, 2016, **88**, 11207–11212.
38 X. Zhong, M. Zhang, L. A. Guo, Y. Xie, R. Luo, W. Chen, F. Cheng and L. Wang, *Biosens. Bioelectron.*, 2021, **189**, 113389.

 This journal is © The Royal Society of Chemistry 2023

Published on 19 avgust 2023. Downloaded on 20. 06. 2025 13:56:39.

39 X. Zhang, J. Peng, Y. Song, Y. Chen, F. Lu and W. Gao, *Biosens. Bioelectron.*, 2019, **133**, 125–132.
40 P. Miao, M. Hao, C. Li, W. Wang, S. Ge, X. Yang, B. Geng, B. Ding, J. Zhang and M. Yan, *Anal. Chim. Acta*, 2022, **1215**, 339990.
41 Z. Liang, H.-Y. Wang, H. Zheng, W. Zhang and R. Cao, *Chem. Soc. Rev.*, 2021, **50**, 2540–2581.
42 K. Chen, J. Xue, Q. Zhou, Y. Zhang, M. Zhang, Y. Zhang, H. Zhang and Y. Shen, *Anal. Chim. Acta*, 2020, **1107**, 145–154.
43 X. Xu, C.-H. Li, H. Zhang and X.-M. Guo, *Nanomaterials*, 2022, **12**, 482.
44 Q. Han, C. Wang, P. Liu, G. Zhang, L. Song and Y. Fu, *Sens. Actuators B Chem.*, 2021, **330**, 129388.
45 X. Ma, C. Pang, S. Li, Y. Xiong, J. Li, J. Luo and Y. Yang, *Biosens. Bioelectron.*, 2019, **146**, 111734.
46 J. Wang, C. Hu, Y.-S. Wang and H. Cui, *ACS Appl. Mater. Interfaces*, 2022, **14**, 3156–3164.
47 X. Xu, H. Wu, X. He, M. K. Hota, Z. Liu, S. Zhuo, H. Kim, X. Zhang and H. N. Alshareef, *ACS Nano*, 2020, **14**, 9840–9847.
48 J. Liu, M. Wang, C. Guo, Z. Tao, M. Wang, L. He, B. Liu and Z. Zhang, *Food Chem.*, 2023, **416**, 135839.
49 M. Hu, L. Zhu, Z. Li, C. Guo, M. Wang, C. Wang and M. Du, *Appl. Surf. Sci.*, 2021, **542**, 148586.
50 X. Xu, H. Wu, X. He, M. K. Hota, Z. Liu, S. Zhuo, H. Kim, X. Zhang and H. N. Alshareef, *ACS Nano*, 2020, **14**, 9840–9847.
51 S. M. Majhi, A. Ali, Y. E. Greish, H. F. El-Maghraby and S. T. Mahmoud, *Sci. Rep.*, 2023, **13**, 3114.
52 J. Liu, M. Wang, C. Guo, Z. Tao, M. Wang, L. He, B. Liu and Z. Zhang, *Food Chem.*, 2023, **416**, 135839.
53 S. Chen, D. Huang, G. Zeng, X. Gong, W. Xue, J. Li, Y. Yang, C. Zhou, Z. Li, X. Yan, T. Li and Q. Zhang, *Chem. Eng. J.*, 2019, **370**, 1087–1100.
54 S. Xu, S. Gong, H. Jiang, P. Shi, J. Fan, Q. Xu and Y. Min, *Appl. Catal., B*, 2020, **267**, 118661.
55 L. Tian, Q. Xin, C. Zhao, G. Xie, M. Z. Akram, W. Wang, R. Ma, X. Jia, B. Guo and J. R. Gong, *Small*, 2021, **17**, 2006530.
56 G. Yang, Y. Zhang, J. Zhao, Y. He, R. Yuan and S. Chen, *Biosens. Bioelectron.*, 2022, **216**, 114629.
57 H. Wu, M. Almalki, X. Xu, Y. Lei, F. Ming, A. Mallick, V. Roddatis, S. Lopatin, O. Shekhah, M. Eddaoudi and H. N. Alshareef, *J. Am. Chem. Soc.*, 2019, **141**, 20037–20042.